Communication

Enhancing Smartphone Satellite Communications by an Antenna Booster

Weihao Diao, Le Chang, Guolong Wang, Yue Li, and Zhijun Zhang

Abstract—**The top metal-frame antenna (TMFA) of a smartphone independently offers limited capacity for satellite communication. This communication proposes a novel antenna booster (AB) technical architecture to enhance channel capacity and communication quality. The AB suppresses the original radiation and redirects energy to a circularly polarized (CP) radiator, significantly enhancing the gain. The AB comprising a monopole coupler (MC) and a CP patch is designed and measured for feasibility verification. Testing on a real-world smartphone shows the proposed AB achieving an impedance bandwidth (IBW) of 18.7% (1.91–2.32 GHz) and an axial ratio bandwidth (ARBW) of 17.6% (1.87–2.32 GHz). In the Tiantong satellite's Tx and Rx bands, it attains a peak gain of 6.1 dBic and an efficiency over 52.9%. The smartphone's CP gain increases by about 6 dB after installing the AB, indicating the feasibility of the architecture.**

Index Terms—**Antenna booster (AB), electromagnetic coupling, energy redirecting, enhanced circularly polarized (CP) gain, satellite communication.**

I. Introduction

In the contemporary world, satellite communication is pivotal for global connectivity, providing versatile options. The rise of satellite communication through mobile phones ensures connectivity in emergencies and areas unreachable by cellular networks.

In satellite communication, circular polarization (CP) is widely adopted to enhance signal stability and resistance to interference. Achieving CP requires two orthogonally polarized electric field components with equal amplitude and a phase difference of 90°. This condition can be met by single feed [1], [2], [3], [4], [5], [6], [7], dual feed [8], [9], [10], [11], and sequentially rotating feed [12], [13], [14], [15], [16]. Besides, CP can be obtained by polarizers [17], [18], [19], helix, and quadrifilar antennas [20], [21].

Satellite phones facilitate satellite communication, incorporating quadrifilar antennas typically [22], [23]. In [24], two cross-shaped folded radiation elements were integrated into a satellite mobile phone, stacked vertically to achieve dual-band circularly polarized (CP) radiation. However, the inconvenience arises from the need to carry both a smartphone and an additional satellite phone.

Compacting smartphone antennas is a popular trend [25], [26]. Various research endeavors have explored the integration of CP antennas into smartphones. For instance, in [27], a multibranch monopole with a parasitic branch on the metal frame of the smartphone is proposed, exciting two orthogonal modes to achieve CP radiation. In [28], a circular patch with radial slots is folded for miniaturization, fed by four L-shaped rotated slots to generate CP. Chang and Liao [29] employ an etched metal sheet placed vertically to the ground plane of the smartphone, exciting two orthogonal modes for CP. In [30], CP is realized with a loop-type element and a monopole-type element, where feeding one element and making the other parasitically resonate excites ground current orthogonally. Zhang et al. [31] proposed a driven dipole and a parasitic dipole on the top of a foldable smartphone with a folding angle of 90° to generate CP. Cao et al. [32] integrated a rectangular loop into the top frame of the smartphone to excite the loop's two orthogonal modes for CP. Zhang et al. [33] utilized a folded cross-dipole to realized CP in the smartphone. However, despite these efforts, spatial constraints on mobile phones often lead to issues, such as narrow IBW, narrow axial ratio bandwidth (ARBW), low gain, or undesired beam pointing for CP antennas on smartphones.

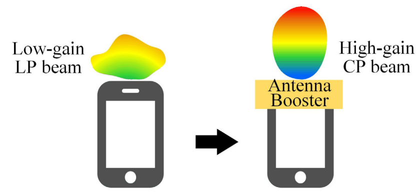

Fig. 1. Schematic of the AB technical architecture.

This communication proposes a novel technical architecture of an antenna booster (AB) to enhance the satellite communication performance of smartphones. The schematic of the architecture is shown in Fig. 1. Working independently, the top metal-frame antenna (TMFA) of the smartphone radiates a low-gain LP beam, providing limited capabilities for only message and audio. However, when multimedia communication is required, the AB is needed. By mounting the AB to the top of the smartphone, the energy originally fed to the TMFA is redirected to a CP radiator, realizing CP radiation, which can achieve wideband [34]. The AB is designed and measured based on a real-world smartphone to verify the workability of the architecture. Due to the wide bandwidth of the dual-feed scheme, the AB exhibits a wide ARBW exceeding 17.6%. Both the −10-dB IBW and the 3-dB ARBW of the proposed AB cover the Tx and Rx frequencies of the Tiantong satellite, with a peak gain of 6.1 dBic and an efficiency exceeding 52.9%. After mounting the AB, the smartphone's CP gain is substantially improved by about 6 dB, proving the practicability of the technical architecture.

Compared to the previous works [30], [31], and [32], the proposed AB design addresses several limitations. Previous CP antennas had limited bandwidth due to the compact size of smartphones. By positioning the AB externally, this limitation can be overcomed, achieving significantly wider bandwidth. The thin form factor of smartphones also limited the gain of internal CP antennas. The AB's larger air-filled patch enhances gain and efficiency. Internal smartphone

Manuscript received 4 March 2024; revised 12 August 2024; accepted 18 August 2024. Date of publication 2 September 2024; date of current version 8 October 2024. This work was supported in part by the National Natural Science Foundation of China under Contract 62271279. *(Corresponding author: Zhijun Zhang.)*

Weihao Diao, Yue Li, and Zhijun Zhang are with Beijing National Research Center for Information Science and Technology (BNRist), Tsinghua University, Beijing 100084, China (e-mail: zjzh@tsinghua.edu.cn).

Le Chang is with the School of Information and Communications Engineering, Xi'an Jiaotong University, Xian 710049, China (e-mail: changle@xjtu.edu.cn).

Guolong Wang is with Honor Device Company Ltd., Beijing 100095, China (e-mail: wangguolong1@hihonor.com).

Color versions of one or more figures in this article are available at https://doi.org/10.1109/TAP.2024.3450329.

Digital Object Identifier 10.1109/TAP.2024.3450329

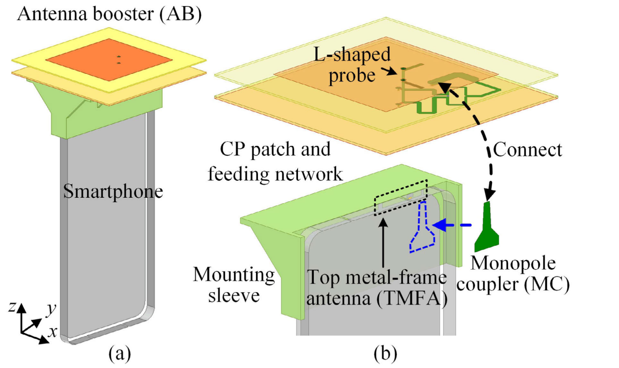

Fig. 2. Assembly relationship between the proposed AB and a smartphone. (a) Assembly diagram. (b) Explosive view.

antennas struggled with precise beam pointing, but the AB's CP patch achieves desired beam pointing by redirecting the smartphone's energy. Furthermore, integrating CP antennas within the limited space of a smartphone often required larger clearances, but the external AB design eliminates such compromises, allowing optimal design without spatial limitations.

The innovations of the proposed work are listed as follows.

1) The AB architecture efficiently suppresses the original radiation and redirects the energy to the CP radiator, which is proposed for the first time in the context of smartphone satellite communication.
2) The feasibility of the proposed architecture is verified by designing the AB in a simple form and testing it with a real-world smartphone. The smartphone's CP gain increases by about 6 dB.

II. AB Configuration and Preparation

A. Configuration of the Proposed AB

Fig. 2 presents the assembly relationship between the proposed AB and a smartphone. For a better illustration, the smartphone in Fig. 2 is simplified as the metal frame and ground. When the AB is mounted, as shown in Fig. 2(a), the energy originally fed to the TMFA will be effectively redirected to the CP patch, boosting the smartphone's satellite communication. The explosive view of the system is shown in Fig. 2(b). The elements from top to bottom in Fig. 2(b) are, respectively, as follows: a square CP patch, two L-shaped probes, a microstrip feeding network, an MC, a mounting sleeve, and a smartphone, respectively. Part of the mounting sleeve is excised for a clearer view. The TMFA, simplified for better demonstration, is marked in the black dashed box. Note that the design does not include the TMFA, but the TMFA must be used to feed the AB. The position of the MC relative to the TMFA after mounting is marked in a blue dashed frame in Fig. 2(b). The geometry of the proposed AB is shown in Fig. 3. As seen in Fig. 3(a), the CP patch is printed on the upper side of an FR4 board ($\varepsilon_r = 4.4$ and $\tan\delta = 0.02$), while the horizontal parts of the L-shaped probes are printed on the lower side. Two metal posts, separated from the patch, serve as the vertical part of the L-shaped probes. The feeding network is printed on the other FR4 board, as depicted in Fig. 3(b). A Wilkinson power divider and a phase shifting line are used to satisfy the feeding requirements of the dual-feed CP patch. A segment of impedance transforming line and two parallel capacitors are employed for matching. At the start of the feeding network, there is a slot-shaped via to connect the MC. The enlarged back view of the via is shown at the upper left of Fig. 3(b) with a red dashed box. There is a gap of $g = 0.35$ mm between the slot-shaped via and the ground. Fig. 3(c) shows the geometry of the MC. Fig. 3(e) illustrates the geometry of the mounting sleeve.

TABLE I
Detailed Dimensions of the Proposed AB

L_g	L_p	L_h	W_h	D_o	D_i	l_1	l_2	l_3	l_4	l_5
80	52.5	9	1.5	2	1.4	21.2	13.4	33.2	3	4
l_6	l_{m1}	l_{m2}	w_1	w_2	w_3	w_4	w_5	H_p	t_p	t_g
3.3	22.2	25.5	4.1	1.5	0.8	2.7	12	7	0.6	0.8
L_{so}	H_{s1}	H_{s2}	T_s	W_{s1}	W_{sf}	W_{so}	W_{si}	L_{si}	L_c	
79	30	13	2	12.4	42.4	52.4	8.4	75	162	

The unit of all parameters is mm.

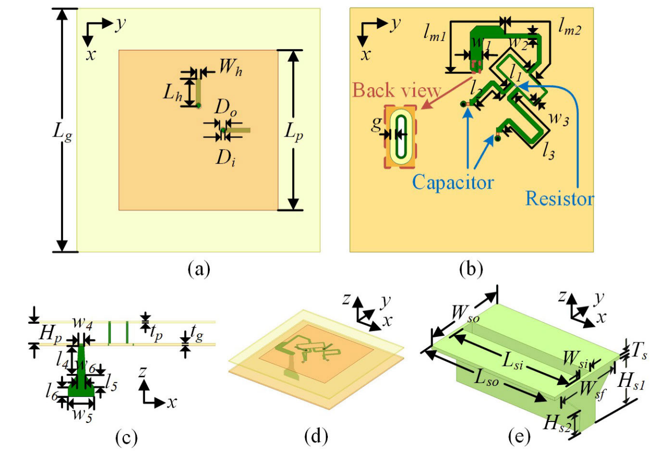

Fig. 3. Geometry of (a) CP patch printed on an FR4 board and (b) feeding network. (c) Side view of the two boards connected with the MC. (d) Perspective view of the boards and MC. (e) Geometry of the mounting sleeve.

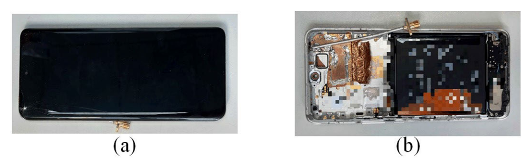

Fig. 4. Photographs of the actual smartphone. (a) Top view (b) Bottom view.

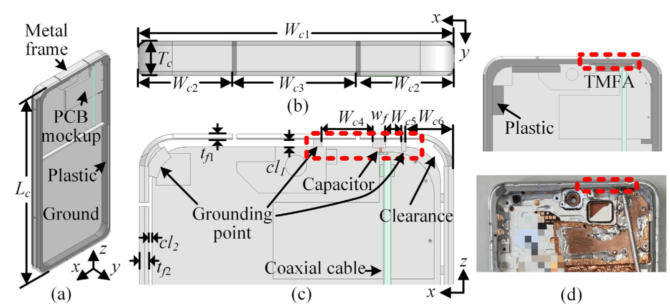

Fig. 5. (a) Perspective view and (b) top view of the modified smartphone. (c) Geometry of the metal frame and ground of the phone. (d) Back views of the actual phone and simulation model.

The sleeve serves to secure the external antenna on the top of the phone. The detailed dimensions of the AB are given in Table I.

B. TMFA Configuration and Simulation Model

To design and test the AB, a real-world smartphone, Honor Magic 4, is used for designing and testing. Fig. 4 displays the photographs of the smartphone. To simplify it, the back cover of the phone has been removed, and the mainboard is replaced by a PCB mockup near the TMFA. To facilitate testing, a coaxial cable is applied to feed the TMFA that is matched by a series capacitor of 1.5 pF. The geometry of the smartphone simulation model is depicted in Fig. 5. The dimensions of the smartphone are given in Table II. The model only considers the TMFA working in the LTE B1 band and

TABLE II
DETAILED DIMENSIONS OF THE SMARTPHONE

W_{c1}	W_{c2}	W_{c3}	T_c	W_{c4}	w_f	W_{c5}	W_{c6}	w6
74	22	29	8	12	3	4.8	10.2	4

The unit of all parameters is mm.

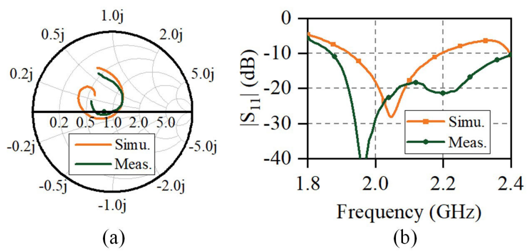

Fig. 6. (a) Smith chart and (b) reflection coefficients of the TMFA in direct feeding.

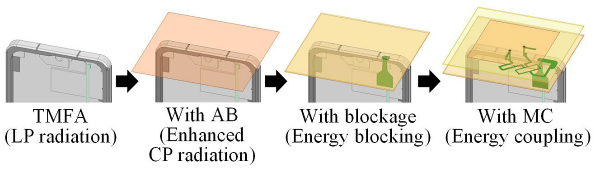

Fig. 7. Design steps of the proposed AB.

adjacent bands, along with detailed structures nearby. The smartphone simulation model was derived based on the test data from an actual smartphone. The final simulation model is shown in Fig. 5(a). The TMFA, marked by red dashed boxes in Fig. 5(c) and (d), is in the form of a driven IFA with a parasitic branch. To demonstrate more clearly, the metal frame and the ground of the phone are shown in Fig. 5(c). The estimated clearances of the top and side frames are $cl_1 = 1.8$ mm and $cl_2 = 0.8$ mm. The width of all the slots on the frame is measured as 1 mm. The measured thickness of the TMFA is $t_{f1} = 1.2$ mm and that of the side frame is $t_{f2} = 2.2$ mm. The back views of the real phone and the simulation model are shown in Fig. 5(d). There is plastic (estimated $\varepsilon_r = 4.5$ and $\tan\delta = 0.01$) connecting the metal frame and the ground. The plastic is in dark gray and the metal frame is in light gray, as shown in Fig. 5(a) and (d). The screen with a thickness of 1.5 mm is represented by a piece of glass (estimated $\varepsilon_r = 4$ and $\tan\delta = 0.01$) in the model, and the ground thickness is 1 mm.

Fig. 6 presents the simulated and measured reflection coefficients of the TMFA. Some additional resonant branches embedded withing the plastic are not included in the simulation. This leads to slightly worse simulated performance compared to the measured data. However, these differences are acceptable in the working band, indicating that the simulation model closely approximates reality.

III. Operating Principle

As shown in Fig. 7, the working principle of the proposed AB can be summarized succinctly: block the original energy radiation and redirect it to the CP radiator for enhanced CP radiation. The design steps are described as follows. First, the TMFA can independently work with LP radiation. Second, with a blockage, the energy originally fed to the TMFA will be totally reflected. Third, with a coupling structure, the blocked energy can be coupled and guided, although it radiates poorly. Finally, by connecting the coupling structure with a CP radiator, the energy can be redirected to the CP radiator for boosted CP radiation, completing the AB. Note that the mounting sleeve is left out as its sole purpose is for the fixture.

To achieve the redirection of the energy, the original radiation must first be suppressed. Connecting the feeding IFA with the parasitic branch using a metal sheet can disrupt the original resonance, effectively suppressing the radiation. The reflection coefficients of the TMFA with different shapes of blockages are plotted in Fig. 8, with the TMFA featuring various blockages shown in the inset. As seen, the reflection coefficients of the TMFA are above −0.5 dB, indicating a high blocking efficiency of above 90%. Thus, as long as the feeding IFA and the parasitic branch are connected, the originally radiated energy will be almost totally reflected.

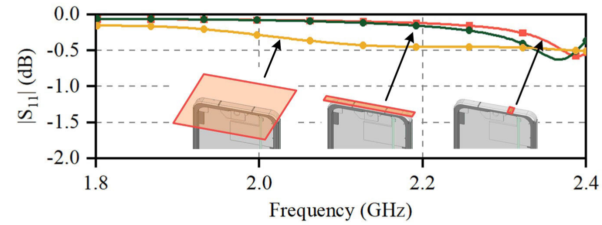

Fig. 8. Reflection coefficients of the TMFA with different shapes of blockage.

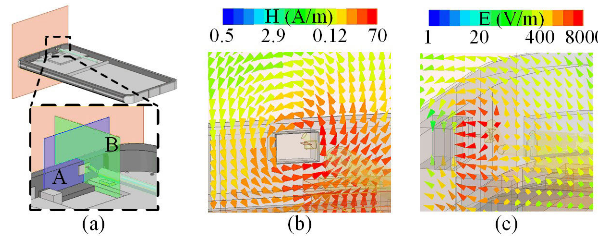

Fig. 9. (a) Planes where the field is plotted. (b) Vector H-field in plane A (the purple plane). (c) Vector E-field in plane B (the green plane).

Subsequently, it is essential to design an appropriate path to smoothly redirect the reflected energy. To effectively guide this energy, a thorough investigation into the field distribution of the blocked TMFA is required. The vector H-field distribution of the TMFA in the plane parallel to the top frame and the vector E-field distribution in the plane perpendicular to the top frame are illustrated in Fig. 9(b) and (c). The planes where the fields are depicted in Fig. 9(a). It is evident that the H-field circulates the feeding point, while the E-field points from the ground toward the protruding part. Based on the analysis above, it can be known that the near-field is akin to that of a monopole. When a monopole, resonant in length, is strategically placed near the feeding point, it facilitates the coupling of energy. Therefore, the coupling structure can be implemented in the form of a monopole coupler (MC). As illustrated in Fig. 10(a) and (b), the MC is positioned directly above the feeding point, with a distance of Dcm = 0.2 mm between the MC and the metal frame. The distance between the central axis of the MC and the side of the smartphone is Lcm = 17 mm. The mounting sleeve is excluded for clarity. To compensate for the shifting of the working band due to the absence of the mounting sleeve, the length of the MC is adjusted. The ground of the MC is the metal sheet used for blockage. A port (Port 2) is introduced between the microstrip line and the ground to observe the efficiency of energy redirecting. The H-field and E-field distributions in the same planes as those in Fig. 9(a) are plotted in Fig. 10(c) and (d). The complex current magnitude distributions on the MC and the metal frame are illustrated in Fig. 10(e) and (f). As observed in Fig. 10(c)–(f), the circling H-field around the feeding point also encompasses the MC, thereby exciting the current on the MC [34], [35]. It is important to note that the MC does not radiate but efficiently couples energy due to its proximity to the ground of the phone. In Fig. 10(d), the E-field is mainly established between the MC and the phone, forming a two-conductor transmission line, resulting in poor radiation from the MC. Owing to the low input impedance of a monopole close to a parallel metal sheet, the port impedance of port 2 is set as 13 Ω. The reflection and the transmission

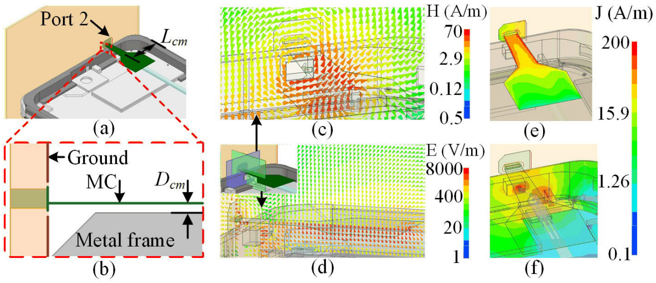

Fig. 10. (a) Configuration and (b) localized enlarged side view of the MC. (c) Vector H-field and vector E-field. (d) Blocked TMFA with the MC. (e) Complex current distribution on the MC and (f) metal frame.

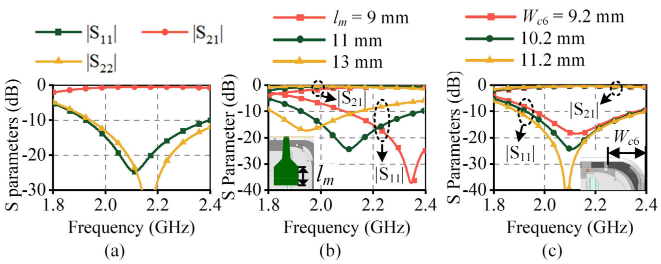

Fig. 11. (a) S-parameters of the blocked TMFA with the MC. (b) S-parameters in different MC lengths and (c) with different grounding positions of the blocked TMFA with the MC.

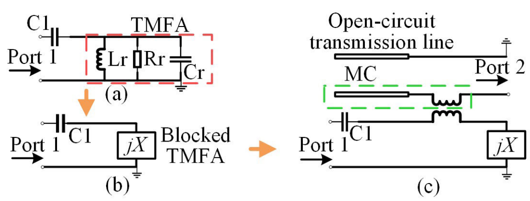

Fig. 12. Working mechanism of the MC expressed in terms of equivalent circuit. Equivalent circuit of (a) TMFA, (b) blocked TMFA, and (c) blocked TMFA with the MC.

coefficients are plotted in Fig. 11. It can be seen that $|S_{11}|$ and $|S_{21}|$ are lower than -10 dB from 1.94 to 2.37 GHz, and $|S_{21}|$ is higher than -1 dB in the same band. Therefore, it can be concluded that the energy redirecting efficiency is high.

The reflection coefficients and transmission coefficients with different lengths l_m of the MC lower part are given in Fig. 11(a). It can be seen that the band of effective energy coupling is shifting with the variance of l_m, indicating that the coupling band is relative to the length of the MC. Fig. 11(b) displays the S-parameters of the TMFA with the coupling structure in different shorting positions W_{c6} of the TMFA. It can be known that the coupling band varies slightly with the variance of W_{c6}. Therefore, the coupling band is primarily determined by the length of the MC. This is because the MC must resonate to couple energy. The MC is positioned close to the ground of the phone, so it forms an open-circuit transmission line with a length of about a quarter wavelength. Hence, the MC can resonate in quarter-wavelength mode to couple energy. On the other hand, the resonance of the TMFA is destroyed completely by connecting the feeding IFA and the parasitic branch, making the blocked TMFA equivalent to a reactance loading. The variance of the grounding position of the feeding IFA only changes the loading effect, so it has little impact on the coupling band.

For an explicit perspective, the working mechanism of the MC expressed in terms of an equivalent circuit is illustrated in Fig. 12. The equivalent circuit of the unblocked and blocked TMFA is depicted in Fig. 12(a) and (b). The capacitor C1 is for impedance matching. The unblocked TMFA is represented by an RLC parallel circuit marked with a red dashed box, while the blocked TMFA is equivalent to a reactance loading jX. Fig. 12(c) presents the equivalent circuit of the blocked TMFA with the MC. The MC marked in the green dashed box and the phone ground together form an open-circuit transmission line in Fig. 12(c). It should be mentioned that the energy is primarily coupled from the protruding part of the TMFA, instead of from the coaxial cable.

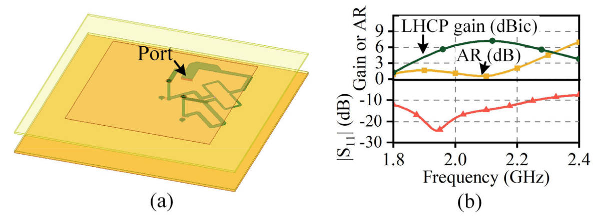

Fig. 13. (a) Geometry and (b) S_{11}, LHCP gain, and AR of the CP patch.

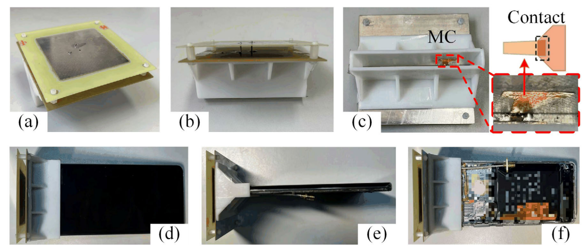

Fig. 14. (a) Three-dimensional view, (b) front view, and (c) bottom view of the AB. (d) Front view, (e) side view, and (f) back view of the AB mounted on the smartphone.

The CP radiator is selected to be a square patch. For a wide bandwidth and a high gain, the height and the edge length of the patch should be large. The geometry of the patch is shown in Fig. 13(a). The distance between the patch board and the feeding network board is 7 mm, making the patch close to an air-filled thick patch. The port is set as 13 Ω to match the output port of the MC. The large thickness contributes to the wide bandwidth, while the large edge length results in high left-handed circular polarization (LHCP) gain, as evident in Fig. 13(b). The wide bandwidth of the Wilkinson power divider and phase shifting line achieves a wideband dual-feed scheme, contributing to the broad ARBW of the CP patch.

IV. Experimental Verification and Discussion

A prototype of the proposed AB was fabricated, as shown in Fig. 14(a)–(c). To solder and secure, the slender part of the MC was implemented using a harder type of copper. The wider part was implemented by cutting the copper tape into the corresponding shape and then adhering it to the inner wall of the mounting sleeve. The connection between the two parts is shown at the upper right of Fig. 14(c). The mounting sleeve was fabricated by 3-D printing, and the relative permittivity of the sleeve is about 5.5. The photographs showing the AB loaded onto the phone are given in Fig. 14(d)–(f). The MC was separated from the phone by 0.2 mm using transparent tape. The distance can be realized in practical processing by covering the MC with an insulating film. The simulated and measured reflection coefficients of the proposed AB mounted on the smartphone are plotted in Fig. 15. The Tx band (1.98–2.01 GHz) and Rx band (2.17–2.2 GHz) of the Tiantong satellite are highlighted with yellow. It can be seen that the working band of the proposed AB in simulation is 1.91–2.31 GHz, while that in measurement is 1.89–2.28 GHz. The difference between the simulation and the measurement is mainly attributed to the imprecise manual cutting of the MC and the estimation of the mounting sleeve's electric parameter. Despite this, the results are sufficient for experimental verification.

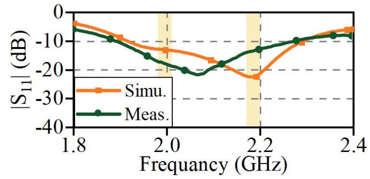

Fig. 15. Reflection coefficient of the AB mounted on the smartphone.

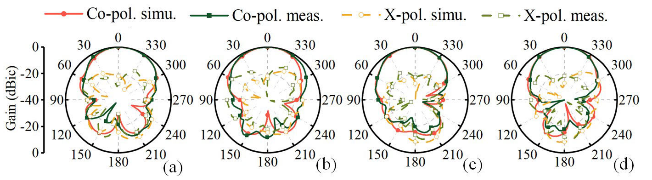

Fig. 16. Normalized radiation patterns of the AB mounted on the phone in different planes at different frequencies. (a) At 2 GHz in the *xoz* plane. (b) At 2 GHz in the *yoz* plane. (c) At 2.19 GHz in the *xoz* plane. (d) At 2.19 GHz in the *yoz* plane.

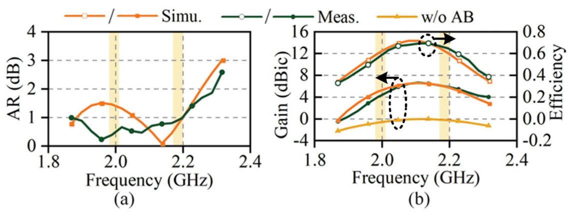

Fig. 17. (a) Axial ratio in the $+z$ direction. (b) Gain in the $+z$ direction and efficiency of the smart phone with and without the AB.

The normalized radiation patterns of the proposed AB mounted on the smartphone in the Tx and Rx bands of the Tiantong satellite are illustrated in Fig. 16. The planes where the radiation patterns are plotted are the *xoz* plane and *yoz* plane. The co-polarization of the AB is LHCP, while right-handed CP is the cross-polarization. As depicted, the maximum gain direction aligns with the $+z$-direction, corresponding to the smartphone's top frame. This alignment facilitates achieving high-capacity and high-quality communication performance when oriented toward the satellite. The simulation and measurement results exhibit good agreement, with any discrepancies attributed mainly to fabrication tolerances and differences between the simulated smartphone and the actual device.

The gain in $+z$-direction, efficiency, and axial ratio of the proposed AB mounted on the smartphone is plotted in Fig. 17. The 3-dB ARBW exceeds 17.6% (1.87–2.32 GHz) due to dual feed. The imperfect contact between the TMFA and the PCB ground in the measurement, the difference between the simulation model and the real phone, and the cable in the anechoic chamber will unpredictably affect the measured AR, leading to the observed differences. In the Tx band of the Tiantong satellite, the LHCP gain is over 4.2 dBic in simulation and 3.6 dBic in measurement, while it surpasses 5.64 dBic in simulation and 5.74 dBic in measurement in the Rx band. In the working band, the simulated peak gain is 5.95 dBic, and the measured peak gain is 6.1 dBic. It should be noted that the contact resistance between the slender part and the wider part of the MC is about 2.5 Ω, which is also considered in the simulation. Without the contact resistance, the peak gain will reach 6.7 dBic, which is not shown for clarity. In the Tx band of the Tiantong satellite, the efficiency is higher than 57.7% in simulation and 52.9% in measurement, while that is over 59.8% in simulation and 64.2% in measurement in the Rx band. The discrepancy is caused by manufacturing tolerance. The LHCP gain of the smartphone at $+z$-direction without the AB is plotted as the yellow line in Fig. 17(b). As seen, the gain of the phone without

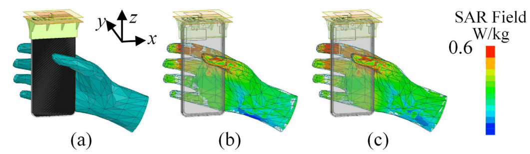

Fig. 18. (a) SAR simulation configuration. SAR of the proposed AB mounted on the smartphone at (b) 2 and (c) 2.19 GHz, averaged over 1 g.

TABLE III

COMPARISON AMONG THE PROPOSED WORK AND OTHER WORKS

Ref.	Type	IBW (%)	ARBW (%)	Max gain (dBic)	Clearance (mm)
[27][1]	Integrated	30 & 12 & 40	5.7	2.7	22 and 8
[28]	Integrated	11.8	3.05	5	N.G.[2]
[29]	Integrated	6.6 & 17	7.9 & 17.3	4.79	40 & 20
[30]	Integrated	6.3	0.6	3	3.5
[31]	Integrated	5.6	0.7	5.9	4
[32]	Integrated	10	0.76	4.8	0.5
[33]	Integrated	1.7	1.5	1.9	2
This work	Antenna booster	18.7	> 17.6%	6.1	-

[1] The impedance BW of [27] is -7.5 dB bandwidth.
[2] N.G.: Not Given.

the AB is lower than 0 dBic across the entire band. In the Tx and Rx bands of the Tiantong satellite, the AB enhances the smartphone's LHCP gain by about 6 dB. Consider the patch board (80 × 80 mm^2) to be the physical aperture. It can be calculated that the aperture efficiencies of the smartphone with the AB in the two bands are, respectively, 73.6% and 84.8%, and that without the AB are 20.7% and 21.5%. The aperture efficiency increases by about three times after mounting the AB. Consequently, the satellite communication performance of the smartphone is significantly boosted. The SAR is analyzed, as shown in Fig. 18, which simulates a scenario where a user is holding a smartphone equipped with the AB in the right hand while communicating with a satellite. The SAR field distributions at 2 and 2.19 GHz in the user's hand with the input power of 24 dBm are displayed in Fig. 18(b) and (c). The SAR values are below 0.42 and 0.54 W/kg at 2 and 2.19 GHz, respectively, which is far lower than the limit of 1.6 W/kg. Because the major amount of energy is redirected to the patch for CP radiation pointing to the $+z$-direction, the user's hand at the back of the AB will absorb little energy. Thus, safe usage can be ensured.

The comparison between the proposed work and other works is presented in Table III. The works referenced for comparison all involve antennas integrated into cell phones. While the antennas in [27] and [28] exhibit a wide IBW, their ARBW is narrow, and the gain is relatively low. The antenna in [29], despite having wide IBW and ARBW, suffers from low gain and includes a large clearance of 20 × 40 mm removed from the ground. In the case of [30], [31], [32], and [33], both IBW and ARBW are narrow. Table III indicates that the proposed AB, when mounted on the smartphone, offers wide IBW and ARBW, high gain, and a defined beam pointing. Thus, the AB can significantly enhance the smartphone's satellite communication, verifying the feasibility of the architecture.

The advantages of wide bandwidth, high gain, and high efficiency require the AB's patch to be air-filled and thick. Additionally, the MC must have a specific length, approximately a quarter wavelength, to function properly. These factors contribute to the relatively larger dimensions. Therefore, miniaturizing the AB while maintaining its advantages is challenging. It is important to note that the current prototype serves as a proof of concept, and the antenna can be designed in other forms. In practical applications, the AB can be designed to be foldable. The proposed AB is suitable for 5G handsets, as most 5G smartphones have TMFAs that cover a wide range of frequencies, including 1.98–2.2 GHz.

V. Conclusion

In this communication, a technical architecture of an AB loaded on the top of a smartphone to significantly improve the smartphone's satellite communication performance is proposed. The AB is designed and measured to verify the feasibility of the architecture, and a smartphone is used for testing. The AB can effectively suppress the original radiation and redirect the energy to the patch for CP radiation. The reflection coefficient of the proposed AB, when mounted on the smartphone, is lower than −10 dB in 1.89–2.28 GHz. In the Tx band (1.97–2.01 GHz) and Rx band (2.17–2.21 GHz) of the Tiantong satellite, the gain surpasses 3.6 and 5.64 dBic, with efficiencies over 52.9% and 64.2%. The 3-dB ARBW exceeds 17.6% (1.87–2.32 GHz). Compared to the smartphone without the AB, the CP gain with the AB can be improved by approximately 6 dB, providing a notable enhancement of channel capacity for boosted satellite communication.

References

[1] D. Sievenpiper, H.-P. Hsu, and R. M. Riley, "Low-profile cavity-backed crossed-slot antenna with a single-probe feed designed for 2.34-GHz satellite radio applications," *IEEE Trans. Antennas Propag.*, vol. 52, no. 3, pp. 873–879, Mar. 2004.

[2] M. Li and K.-M. Luk, "A wideband circularly polarized antenna for microwave and millimeter-wave applications," *IEEE Trans. Antennas Propag.*, vol. 62, no. 4, pp. 1872–1879, Apr. 2014.

[3] J.-I. Oh, H.-W. Jo, K.-S. Kim, H. Cho, and J.-W. Yu, "A compact cavity-backed slot antenna using dual mode for IoT applications," *IEEE Antennas Wireless Propag. Lett.*, vol. 20, pp. 317–321, 2021.

[4] K. Kumar, S. Dwari, and M. K. Mandal, "Broadband dual circularly polarized substrate integrated waveguide antenna," *IEEE Antennas Wireless Propag. Lett.*, vol. 16, pp. 2971–2974, 2017.

[5] W.-T. Hsieh, T.-H. Chang, and J.-F. Kiang, "Dual-band circularly polarized cavity-backed annular slot antenna for GPS receiver," *IEEE Trans. Antennas Propag.*, vol. 60, no. 4, pp. 2076–2080, Apr. 2012.

[6] C. Deng, Y. Li, Z. Zhang, G. Pan, and Z. Feng, "Dual-band circularly polarized rotated patch antenna with a parasitic circular patch loading," *IEEE Antennas Wireless Propag. Lett.*, vol. 12, pp. 492–495, 2013.

[7] Y. Li, Z. N. Chen, X. Qing, Z. Zhang, J. Xu, and Z. Feng, "Axial ratio bandwidth enhancement of 60-GHz substrate integrated waveguide-fed circularly polarized LTCC antenna array," *IEEE Trans. Antennas Propag.*, vol. 60, no. 10, pp. 4619–4626, Oct. 2012.

[8] J. Shi, X. Wu, X. Qing, and Z. N. Chen, "An omnidirectional circularly polarized antenna array," *IEEE Trans. Antennas Propag.*, vol. 64, no. 2, pp. 574–581, Feb. 2016.

[9] X. Ding, Z. Zhao, Y. Yang, Z. Nie, and Q. H. Liu, "A compact unidirectional ultra-wideband circularly polarized antenna based on crossed tapered slot radiation elements," *IEEE Trans. Antennas Propag.*, vol. 66, no. 12, pp. 7353–7358, Dec. 2018.

[10] G. Srivastava and A. Mohan, "A differential dual-polarized SIW cavity-backed slot antenna," *IEEE Trans. Antennas Propag.*, vol. 67, no. 5, pp. 3450–3454, May 2019.

[11] R. K. Saini and S. Dwari, "A broadband dual circularly polarized square slot antenna," *IEEE Trans. Antennas Propag.*, vol. 64, no. 1, pp. 290–294, Jan. 2016.

[12] J. Wu, M. Li, and N. Behdad, "A wideband, unidirectional circularly polarized antenna for full-duplex applications," *IEEE Trans. Antennas Propag.*, vol. 66, no. 3, pp. 1559–1563, Mar. 2018.

[13] S. X. Ta and I. Park, "Compact wideband sequential-phase feed for sequentially rotated antenna arrays," *IEEE Antennas Wireless Propag. Lett.*, vol. 16, pp. 661–664, 2017.

[14] C. Ma, Z.-H. Ma, and X. Zhang, "Millimeter-wave circularly polarized array antenna using substrate-integrated gap waveguide sequentially rotating phase feed," *IEEE Antennas Wireless Propag. Lett.*, vol. 18, pp. 1124–1128, 2019.

[15] Y. Shen, S.-G. Zhou, G.-L. Huang, and T.-H. Chio, "A compact dual circularly polarized microstrip patch array with interlaced sequentially rotated feed," *IEEE Trans. Antennas Propag.*, vol. 64, no. 11, pp. 4933–4936, Nov. 2016.

[16] Y. Zhang, Y. Li, M. Hu, P. Wu, and H. Wang, "Dual-band circular-polarized microstrip antenna for ultrawideband positioning in smartphones with flexible liquid crystal polymer process," *IEEE Trans. Antennas Propag.*, vol. 71, no. 4, pp. 3155–3163, Apr. 2023.

[17] Z. L. Ma and X. F. Xiao, "Additively manufactured dual circularly polarized antennas with bidirectional same-sense radiation and wide bandwidth characteristics," *IEEE Trans. Antennas Propag.*, vol. 71, no. 1, pp. 1029–1034, Jan. 2023.

[18] K. X. Wang and H. Wong, "A wideband millimeter-wave circularly polarized antenna with 3-D printed polarizer," *IEEE Trans. Antennas Propag.*, vol. 65, no. 3, pp. 1038–1046, Mar. 2017.

[19] P. Wang et al., "Circularly polarized polarization conversion metasurface-inspired antenna array with low RCS over a wide band," *IEEE Trans. Antennas Propag.*, vol. 71, no. 7, pp. 5626–5636, Jul. 2023.

[20] Z. Chen, Z. Hu, J. Zhang, G. Zhang, and C. Guo, "Compact normal-mode hybrid-helix antenna and its application to circularly polarized Yagi array," *IEEE Trans. Antennas Propag.*, vol. 69, no. 9, pp. 5986–5991, Sep. 2021.

[21] Y. Tawk, M. Chahoud, M. Fadous, J. Costantine, and C. G. Christodoulou, "The miniaturization of a partially 3-D printed quadrifilar helix antenna," *IEEE Trans. Antennas Propag.*, vol. 65, no. 10, pp. 5043–5051, Oct. 2017.

[22] A. M. Musthafa, M. Khalily, A. Araghi, O. Yurduseven, and R. Tafazolli, "Compact multimode quadrifilar helical antenna for GNSS-R applications," *IEEE Antennas Wireless Propag. Lett.*, vol. 21, pp. 755–759, 2022.

[23] Y.-S. Wang and S.-J. Chung, "A miniature quadrifilar helix antenna for global positioning satellite reception," *IEEE Trans. Antennas Propag.*, vol. 57, no. 12, pp. 3746–3751, Dec. 2009.

[24] H. R. Lee, H. K. Ryu, S. Lim, and J. M. Woo, "A miniaturized, dual-band, circularly polarized microstrip antenna for installation into satellite mobile phones," *IEEE Antennas Wireless Propag. Lett.*, vol. 8, pp. 823–825, 2009.

[25] L. Chang and H. Liu, "Low-profile and miniaturized dual-band microstrip patch antenna for 5G mobile terminals," *IEEE Trans. Antennas Propag.*, vol. 70, no. 3, pp. 2328–2333, Mar. 2022.

[26] L. Chang and H. Wang, "Miniaturized wideband four-antenna module based on dual-mode PIFA for 5G 4 × 4 MIMO applications," *IEEE Trans. Antennas Propag.*, vol. 69, no. 9, pp. 5297–5304, Sep. 2021.

[27] Z. Liang, Y. Li, and Y. Long, "Multiband monopole mobile phone antenna with circular polarization for GNSS application," *IEEE Trans. Antennas Propag.*, vol. 62, no. 4, pp. 1910–1917, Apr. 2014.

[28] K. M. Mak, H. W. Lai, K. M. Luk, and C. H. Chan, "Circularly polarized patch antenna for future 5G mobile phones," *IEEE Access*, vol. 2, pp. 1521–1529, 2014.

[29] S.-H. Chang and W.-J. Liao, "A novel dual band circularly polarized GNSS antenna for handheld devices," *IEEE Trans. Antennas Propag.*, vol. 61, no. 2, pp. 555–562, Feb. 2013.

[30] L. Qu and H. Kim, "A novel single-feed dual-element antenna using phase compensation and magnitude regulation to achieve circular polarization," *IEEE Trans. Antennas Propag.*, vol. 66, no. 10, pp. 5098–5108, Oct. 2018.

[31] X. Zhang, K. Wei, Y. Li, and Z. Zhang, "A polarization reconfigurable antenna for satellite communication in foldable smartphone," *IEEE Trans. Antennas Propag.*, vol. 71, no. 12, pp. 9938–9943, Dec. 2023.

[32] Z. Cao, L. Chang, Y. Li, K. Wei, and Z. Zhang, "Compact mobile terminal antenna with endfire circularly polarized beam for satellite communications," *IEEE Trans. Antennas Propag.*, vol. 71, no. 12, pp. 9980–9985, Dec. 2023.

[33] X. Zhang, K. Wei, Y. Li, and Z. Zhang, "A circularly polarized antenna based on narrowed crossed dipole for smartphone satellite communication," *IEEE Antennas Wireless Propag. Lett.*, vol. 23, pp. 2511–2515, 2024.

[34] Y. Zhang and Y. Li, "Wideband microstrip antenna in small volume without using fundamental mode," *Electromagn. Sci.*, vol. 1, no. 2, Jun. 2023, Art. no. 0020073.

[35] C. A. Balanis, *Antenna Theory: Analysis and Design*. Hoboken, NJ, USA: Wiley, 1997.

[36] M. K. Krage and G. I. Haddad, "Characteristics of coupled microstrip transmission lines—I: Coupled-mode formulation of inhomogeneous lines," *IEEE Trans. Microw. Theory Techn.*, vol. MTT-18, no. 4, pp. 217–222, Apr. 1970.